

Modeling and interpretation of tweed microstructures in face-centered-cubic solids

A. Silberstein and P. C. Clapp

Department of Metallurgy and Institute of Materials Science, University of Connecticut, Storrs, Connecticut 06268

(Received 25 February 1988)

Using molecular-dynamics simulations and an interatomic potential that had been designed to be unstable to $\langle 110 \rangle \{1\bar{1}0\}$ shears, we studied the mechanisms of tweed formation in face-centered-cubic (fcc) crystals. We found that tweed is most probably a premartensitic phenomenon that nucleates homogeneously in strongly anharmonic solids. Yet tetragonal strain fields will enhance the formation of tweed in the crystal. Unlike the case of body-centered-cubic (bcc) crystals, we did not find any particular feature in the interatomic potential that is common to all materials showing a tweed instability. Finally, we showed that solitons with hyperbolic-tangent strain fields are the kind of elastic shear waves that propagate in such anharmonic solids.

I. INTRODUCTION

Since its first characterization in relation to Guinier-Preston (GP) zone formation in Cu-Be alloys by Tanner¹ in 1966 as spontaneous tetragonal distortions of a cubic lattice, "tweed" has attracted considerable attention because of its possible connection to the nucleation of the martensite phase. With the sudden new advances in the field of superconductors, the tweed phenomenon has rearoused the interest of many researchers. Indeed, it has been suggested^{2,3} that tweed, or rather tetragonal distortions of the lattice, might be the basis for the superconducting effect in Y-Ba-Cu-O and Ba-La-Cu-O perovskite compounds, through its influence on the electron-phonon coupling in these materials. However, the fundamentals of the phenomenon are still not fully understood.

In the course of an extensive study of tweed in Ni-Al alloys, Robertson and Wayman⁴ proposed the following definition of the term. "Tweed describes linear variations in contrast which lie approximately parallel to the traces of $\{110\}$ planes of a nominally cubic solid solution, and which obey extinction rules consistent with $[1\bar{1}0]\{110\}$ shear displacements."

Apart from being associated with GP zone formation, tweed microstructures have also often been observed in systems undergoing martensitic transformations. Most of the observations were made on bcc alloys, such as NiAl,⁴ Cu-Al-Ni, and Cu-Zn,⁵ but there is evidence of tweed occurring in fcc alloys as well [Fe-Ni alloys (Refs. 6 and 7), and Ni₃Al (Ref. 8)]. In most cases, the appearance of tweed is concurrent with other anomalous phenomena, such as lattice softening and anomalous phonon dispersion, that also appear in the vicinity of the M_s temperature upon cooling from higher temperature, or in the vicinity of the A_s temperature upon heating of the sample. This is what led various authors^{5,6} to conclude that large amplitude vibrations were responsible for the diffracted streaks characteristic of tweed microstructures.

The theories on tweed formation can basically be divided into two categories. (1) one category includes theories that suppose that tweed originates from static causes, such as shears produced around defects, precipitates, local ordering, or GP zones. Those have been invoked in

particular by Tanner¹ and Wen *et al.*⁹ In that case, lattice anisotropy seems to be the major cause of the appearance of tweed contrast. (2) Another category concerns theories that suppose that the origin of tweed is essentially dynamic, caused by phonon softening and anharmonicity, which have occurred in relation to premartensitic phenomena. In fact, when tweed occurs prior to a martensitic transformation, it has in some cases been possible to prove that its formation is not caused by second-phase precipitation.⁸

Delacy *et al.*¹⁰ pointed out that the magnitude of $C' = \frac{1}{2}(C_{12} - C_{12})$ (at least for the Hume-Rothery β phases) is very sensitive to uniaxial stresses, and Guénin and Gobin¹¹ showed that this may lead to values locally equal to, or very close to, zero due to the strains involved near lattice discontinuities (such as dislocations, grain boundaries, point defects, etc.). This process could be one of the causes for a C' lattice instability. Another suggestion derives from the observation that many of the alloys that show tweed also have a very high elastic anisotropy in that temperature range, so that the strain created around small tetragonal precipitates is quite large. A different explanation applies to the family of ferromagnetic invar alloys such as Fe-Ni and Fe-Ti alloys. In that case, the marked softening of the lattice has been related to the magnetic properties of those alloys, since no elastic softening occurs if $T_c \leq M_s$ (where T_c is the Curie temperature).¹²

Lattice anharmonicity and softening have also very often been invoked for the interpretation of tweed behavior in reciprocal space. For instance, diffuse scattering effects have been interpreted in terms of transverse $\langle 110 \rangle$ fluctuation waves of displacements characterized by extensive two-dimensional regions parallel to $\{110\}$ planes.^{5,6} They have also been described as the manifestation of the tetragonal transformation of the austenite phase upon the action of a double $\langle 1\bar{1}0 \rangle_\gamma \{110\}_\gamma$ shear.¹³ This latter point suggests the appearance of tweed as a premartensitic effect, the tweed microstructure being intermediate between the microstructures of the austenite and the martensite. However, up to now there is no proof that this might indeed be the case.

In addition to those experimental results, some com-

puter experiments have been performed to try to shed some light upon the nature of tweed. Using a Monte Carlo simulation algorithm, Wen *et al.*⁹ looked at the most stable configuration that randomly dispersed tetragonal precipitates in an idealized elastic cubic matrix would assume. They showed that under such assumptions, the energetically favorable configuration of the precipitates is to align along $\langle 110 \rangle$ directions of the matrix. They calculated that this configuration reproduces fairly accurately the experimental diffraction pattern, as well as the observed bright-field imaging oscillation contrast, thus proving that tweed is the result of an attempt to minimize the elastic energy produced by an array of tetragonal precipitates. In an attempt to understand the mechanisms of tweed formation, Clapp *et al.*¹⁴ ran molecular-dynamics simulations using an interatomic potential that had been specifically calculated to produce a bcc lattice unstable with respect to $\langle 1\bar{1}0 \rangle \{110\}$ shear strains. They were able to reproduce $\langle 110 \rangle$ streaking in the diffraction patterns and found that point defects such as interstitials (which produce a tetragonal strain field in a bcc lattice) increased the tweed effect, i.e., streaking was more marked and appeared at higher temperature, whereas vacancies (which have a cubic strain field) had not noticeable influence as compared to the perfect crystal response. The simulated crystal underwent a homogeneous martensitic transformation at low temperature, but no attempt was made to relate that transformation to the tweed phenomenon itself.

As mentioned previously, lattice anharmonicity can very often be associated with the presence of a tweed instability. It is interesting to note here the analysis made by Krumhansl and Schrieffer¹⁵ who showed that when the interactions between the particles in a solid are strongly anharmonic, then the displacements of those particles can no longer be adequately represented by the usual phonon waves or phonon perturbation approximation. They calculated that (following their terminology) *domain walls* are an important type of excitation in one-dimensional systems which result directly from the anharmonicity of the system, and which produce a central peak in the phonon spectrum that has been observed experimentally to accompany the appearance of a soft-mode in the course of structural phase transitions. Those domain walls, which have been shown by computer simulation to link small clusters of locally distorted regions, can be described by

$$u = u_0 \tanh \left[\frac{1}{\sqrt{2}} \frac{(x - vt)}{\xi} \right], \quad (1)$$

where u is the displacement of the particles, u_0 is the amplitude of the displacement at $\pm \infty$ [the displacement is $+u_0$ if $(x - vt) > 0$ and is $-u_0$ if $(x - vt) < 0$], and v is the velocity of the wall, which has a thickness $2\sqrt{2}\xi$.

In the next section of this paper, we describe the model and assumptions used to simulate a tweed instability in the computer. In particular, we assumed that the fcc lattice had to be strongly anharmonic, and unstable with respect to $\langle 110 \rangle \{1\bar{1}0\}$ shears. We also detail the method used to calculate an interatomic potential appropriate for

the molecular-dynamics simulations.

In Sec. III we present the results obtained during the simulation experiments. We were able to observe tweed in a temperature range $T < T_m/5$ (where T_m is the approximate melting temperature of our system), and the effect of various defects on the phenomenon. An analysis based on the various energies of the waves has been performed to try to determine exactly what kind of shear wave was propagating in our anharmonic solid. We found that a new kind of soliton that produces a hyperbolic tangent strain field was the energetically most favorable in our system, and those results will be discussed in Sec. IV.

II. MODELING

The displacements that show up as tweed during electron imaging of the crystals can be thought of as small tetragonal distortions in the cubic matrix. Our approach was to construct a lattice in the computer that, due to the interatomic potential chosen, exhibits a tetragonal instability, and specifically a $\langle 1\bar{1}0 \rangle \{110\}$ shear instability, since the combination of two of those shears of the same amplitude is equivalent to a tetragonal distortion.

A. Model for the lattice potential energy

Such a requirement implies a strong anharmonicity of the lattice, which shows as a negative second derivative of the potential energy with respect to the strain parameter of interest. We assumed that the potential energy of a system that shows tweed can be adequately represented as a function of a strain parameter by the curve shown in Fig. 1. This double-minimum curve simply means that a slightly strained configuration of the crystalline lattice is energetically more stable than the unstrained fcc lattice.

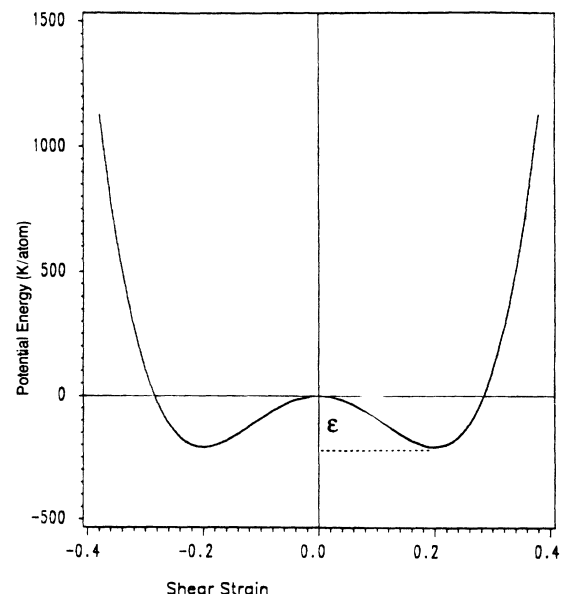


FIG. 1. Model assumed for the lattice potential energy as a function of strain. ϵ is the height of the energy barrier for straining the lattice.

In particular, one can speculate that the free energy of our system (which becomes the same as the potential energy at absolute zero) will evolve as a function of temperature following these key steps.

(i) If $kT < \varepsilon$, the height of the energy barrier, the crystal will spend a substantial amount of time in a strained configuration, since the kinetic energy will not be large enough to surmount the free-energy barrier. A diffraction pattern taken from such a structure will exhibit Bragg peaks shifted because of the homogeneous strain that the lattice undergoes, with some diffuse scattering that accounts for thermal fluctuations around that position.

(ii) If $kT \approx \varepsilon$, there is a finite probability for the system to surmount the energy barrier, and the crystal will keep switching from one strained configuration to the next, depending on whether it is trapped in one or the other of the two minima. The intensity of the Bragg diffraction peaks, in this case, should be split symmetrically on either side of the Bragg position to a position that corresponds approximately to the amount of strain at the minimum.

(iii) If $kT > \varepsilon$, the lattice should behave on average as a regular fcc lattice, and the diffraction pattern should show peaks at the regular Bragg positions.

Even though the quantitative determination of the free energy of a system as a function of temperature is a rather complicated process even with the use of molecular-dynamics simulations (see, for example, Ref. 16), we expect to be able to test our hypothesis at least qualitatively by examining the resulting diffraction patterns and radial distribution functions of the lattice at different temperatures.

B. Analytical expression for the potential energy E

Because of the periodicity of a crystalline lattice, the lattice potential energy must also be periodic as a function of strain if the strain is itself a periodic function (as are, for example, pure shear strains, as opposed to dilational strains). As a result, we can expand the function describing the potential energy versus $\langle 1\bar{1}0 \rangle \{110\}$ strain in a Fourier series:

$$E(\eta) = \sum_{n=0}^{\infty} A_n \cos \left[\frac{2\pi n \eta}{\eta_0} \right] + \sum_{n=0}^{\infty} B_n \sin \left[\frac{2\pi n \eta}{\eta_0} \right], \quad (2)$$

where η is the shear-strain parameter (taken as the ratio of the shear displacement of any plane to its distance from the origin), and η_0 is the period ($\eta_0 = 2$ in our case as a consequence of the fcc symmetry).

But our choice of a model with a symmetric double minimum around $\eta = 0$ implies an even function, so

$$E(\eta) = \sum_{n=0}^{\infty} A_n \cos \left[\frac{2\pi n \eta}{\eta_0} \right]. \quad (3)$$

It is shown in the Appendix that the simplest expansion of $E(\eta)$ that will reproduce the desired features of the curve can be limited to the three first terms: $n = 0, 1, 2$. We chose arbitrarily the value of the strain at the minimum to be $\eta_{\min} = 0.2$, and the height of the energy barrier ε to be equal to 211.28 K (for convenience, all the

energies have been divided by the Boltzmann constant and are expressed in degrees Kelvin). The potential energy curve was then expressed as

$$E(\eta) = 6489.43 - 9391.68 \cos(\pi\eta) + 2902.25 \cos(2\pi\eta). \quad (4)$$

C. Calculation of the interatomic potential

Once the potential energy curve has been determined, we can calculate an interatomic potential that will produce the desired tetragonal instability. The energy of interaction of individual atoms within a crystalline lattice is described as a function of distance by the interatomic potential curve. Assuming only central forces are present, the potential energy of a lattice is equal to the sum of all the pairwise interaction energies:

$$E = \frac{1}{2} \sum_{i,j} V(r_{ij}), \quad (5)$$

where i and j represent, respectively, all the atoms in the lattice, $r_{ij} = |\mathbf{r}_i - \mathbf{r}_j|$ is the distance between atom i and its j th neighbor, $V(r_{ij})$ is the value of the pairwise potential at a distance r_{ij} between atoms. The factor $\frac{1}{2}$ corrects for counting each pair of atoms twice.

In our particular problem, the total potential energy E is a function of the strain parameter η , as is also r_{ij} . Therefore, in order to obtain the pair potential curve, the following system of equations has to be solved in $V(r)$:

$$\begin{aligned} E(\eta_1) &= \frac{1}{2} \sum_{i,j} V(r_{ij}(\eta_1)), \\ E(\eta_2) &= \frac{1}{2} \sum_{i,j} V(r_{ij}(\eta_2)), \\ &\vdots \\ E(\eta_m) &= \frac{1}{2} \sum_{i,j} V(r_{ij}(\eta_m)), \end{aligned} \quad (6)$$

where the η_m 's are discrete values of the strain parameter chosen so as to give a good representation of the shape of the curve $E(\eta)$. If the η_m 's are chosen at sufficiently close values, the equations above should lead to a unique function $V(r)$ in the range $r_{\min} \leq r \leq r_c$, where r_{\min} is the distance of closest approach between atoms during shear, and r_c is the assumed cutoff distance for $V(r)$. For an fcc lattice in homogeneous $\langle 110 \rangle \{1\bar{1}0\}$ shear, $r_{\min} = \sqrt{3}a_0/2\sqrt{2}$.

We then assumed that $V(r)$ could be expanded in a power series:

$$V(r) = \sum_{n=0}^{p-1} a_n r^{n-n_0}, \quad (7)$$

where the parameters are p (the length of the series) and n_0 (the initial power), and the a_n 's are to be determined.

Additional constraints were imposed on $V(r)$ in view of the computer simulation. In particular, we truncated the interatomic potential at a cutoff radius r_c half-way between the third- and fourth-neighbor distances. In order

to help in the simulation algorithm, we imposed a value of zero for the potential and its first derivative at r_c . Finally, in order to simulate physical systems, we had to ensure that the system would be stable at its nominal atomic volume (i.e., it would not spontaneously collapse or dissociate). For that purpose, we used a stability condition derived by Maeda *et al.*¹⁷ and assuming no volume forces are applied to the system, it may be written as

$$\sum_{\substack{j=1 \\ (j \neq i)}}^N r_{ij} \frac{\partial V(r_{ij})}{\partial r_{ij}} = 0, \quad (8)$$

where N is the total number of atoms. The system of equations now transforms to

$$\begin{aligned} E(\eta_1) &= \frac{1}{2} \sum_n a_n \sum_{i,j} [r_{ij}(\eta_1)]^{n-n_0}, \\ E(\eta_2) &= \frac{1}{2} \sum_n a_n \sum_{i,j} [r_{ij}(\eta_2)]^{n-n_0}, \\ &\vdots \\ E(\eta_m) &= \frac{1}{2} \sum_n a_n \sum_{i,j} [r_{ij}(\eta_m)]^{n-n_0}, \\ 0 &= \sum_n a_n [r_c(0)]^{n-n_0}, \\ 0 &= \sum_n (n-n_0) a_n [r_c(0)]^{n-n_0-1}, \\ 0 &= \sum_n (n-n_0) a_n \sum_{i,j} [r_{ij}(0)]^{n-n_0}. \end{aligned} \quad (9)$$

This $(m+3) \times p$ system of linear equations was then solved for the a_n 's using a least-square analysis.

III. RESULTS AND DISCUSSION

A. Interatomic potential

We found that a minimum number of elements in the series expansion of the interatomic potential $p \geq 7$ had to be used to ensure the reproduction of the potential energy curve, which was then duplicated with an accuracy of $\pm 1\%$. The interatomic potential that we chose for the computer simulations is

$$V(r) = \sum_{n=0}^8 a_n r^{n-1} \quad (10)$$

and is represented in Fig. 2. The cutoff radius was chosen half-way between the third and fourth neighbors at $r_c = 1.32$ fcc unit cell lengths, and the corresponding coefficients a_n of the power series are given in Table I.

The behavior of this system as a function of a homogeneous expansion or contraction of the lattice is shown in Fig. 3. It can be seen from that figure that this potential makes both the fcc and the bcc phases stable, which is a requirement to be able to simulate both lattices in the CMD (Computer Molecular Dynamics) program, and furthermore that the bcc phase (with an energy of -1938.70 K/atom) is, at least at 0 K, thermodynamically more stable than the fcc phase (whose corresponding energy is -28.09 K/atom), which indicates a driving

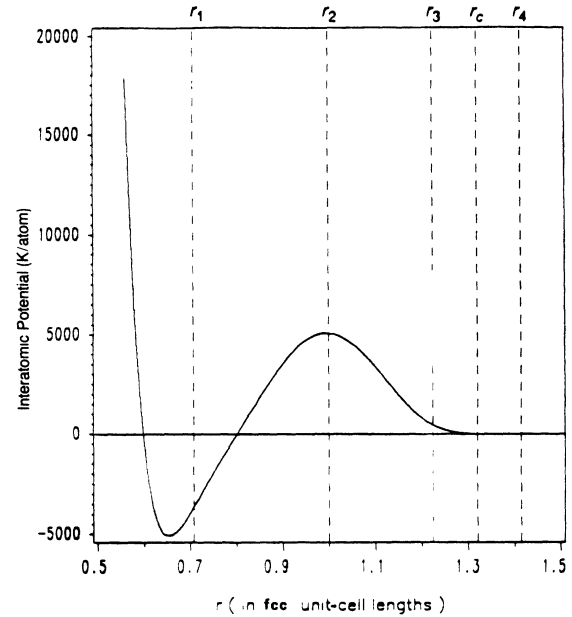


FIG. 2. Interatomic potential that produces a C' instability. The r_n 's ($n=1-4$) represent the positions of the four first fcc neighbors, and $r_c = 1.32$ is the cutoff distance. The interatomic distance is expressed in terms of the fcc lattice parameter, and the potential is in units of degrees Kelvin (with multiplication by Boltzmann's constant understood).

force toward a phase transformation. It is noteworthy that a majority of the interatomic potentials that we calculated also showed this tendency for a low-temperature transformation. The calculation of the first and second derivatives at the successive neighbor positions has been performed systematically for all the calculated interatomic potentials, but no obvious trend has been found that could be invoked as a feature common to all fcc systems that show tweed, as had been the case during the study of bcc alloys.¹⁴

B. Simulation results

Simulation runs were done systematically from 10 to 7000 K. Such a wide temperature range has been chosen in order to characterize the system under simulation, in particular to find the melting temperature, observe the occurrence of any phase transformation, and determine

TABLE I. Coefficients of the series expansion of the interatomic potential.

n	a_n
0	1.1961×10^4
1	-2.8722×10^4
2	2.9845×10^4
3	-1.7519×10^4
4	6.3507×10^3
5	-1.4552×10^3
6	2.0579×10^2
7	-1.6423×10^1
8	5.6643×10^{-1}

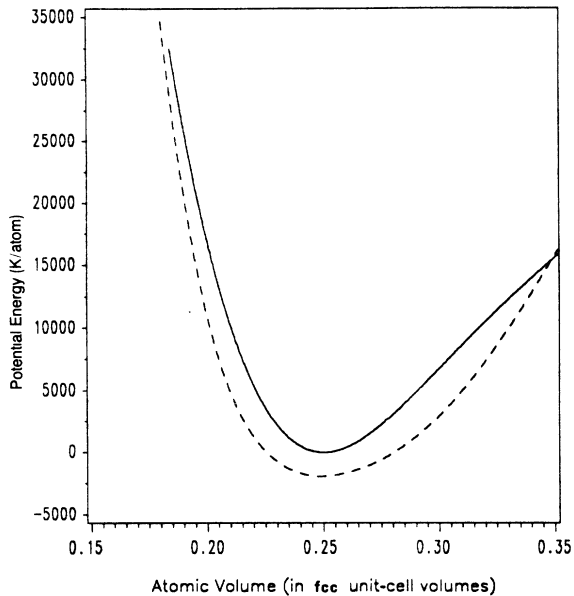


FIG. 3. Behavior of the lattice potential as a function of the atomic volume. The atomic volume is expressed in terms of the fcc parameter. The solid line represents the fcc phase, and the dashed line represents the bcc phase.

the tweed behavior as a function of temperature. Various defects artificially put into the perfect lattice array have been tested in addition to the perfect lattice: a vacancy, an interstitial, a tilt boundary, and a vacancy loop. The initial relative orientation of the fcc particle array and the simulation box has to be chosen relative to the instability that we seek to observe, a consequence of the periodic boundary conditions used in the molecular-dynamics program in order to minimize the effect of free surfaces on the system. Indeed, homogeneous particle displacements in directions nonparallel to the orientation of the simulation box will be prohibited because the periodicity of the lattice would be broken upon application of the periodic boundary conditions. For the $\langle 110 \rangle \{1\bar{1}0\}$ shear, the box was oriented along the $\langle 110 \rangle$ directions of the fcc lattice, i.e.,

$$X_{\text{box}} \equiv [110], \quad Y_{\text{box}} \equiv [1\bar{1}0], \quad Z_{\text{box}} \equiv [001]. \quad (11)$$

A perfect array of 640 particles was fitted into the box, i.e., there were four fcc unit cells in both the X and Y directions of the box, and five unit cells in the Z direction.

An interstitial was created by simply adding one particle in an empty octahedral site of the lattice, a vacancy by removing one of the particles of the array, and a vacancy loop was produced by removing part of a $(1\bar{1}0)$ atomic plane, parallel to one side of the box, so as to produce a semi-infinite (in the Z direction) planar defect. Therefore, the array contained 641 particles when an interstitial was added to the perfect lattice, 639 particles in the case of a vacancy, and 620 particles when a vacancy loop was created.

For each of those defects, we ran a “presimulation” simulation of 1000 steps at 1 K to allow the defects to statically relax before running any simulation at higher

temperature. The relaxed configurations were then input as *step 0* into the CMD program.

The melting temperature T_m of our system was determined from the discontinuity that occurs in the potential energy versus temperature curve at the melting point. It was found to vary by as much as 20% depending on the defect simulated in the lattice, from about 5000 K with the vacancy loop to about 6000 K for the perfect infinite crystal. However surprising at first, such a large variation in the melting point can be rationalized if one considers that under periodic boundary conditions free surfaces, which are among the most effective heterogeneous nucleation sites for the melting transition, are completely absent. We are, therefore, looking at the melting transition under quasihomogeneous nucleation conditions, where high-energy defects such as the tilt boundary or defects that produce some free volume such as the vacancy loop are expected to ease considerably the melting process. Also, since the simulations are run at constant volume, the volume increase that would be expected upon melting is rather translated into an increase in pressure of the system, unless there is enough free volume to release this pressure, thereby increasing the melting point from what it would be under adiabatic conditions.

1. Effect of temperature on tweed

The mean-square displacement (MSD) is a good representation of the magnitude of the atomic motions in the system and/or of the number of particles that participate in the motions and may be directly related to the Debye-Waller factor in x-ray measurements or the recoilless fraction in Mössbauer experiments. The “averaged MSD,” a time average of the MSD at a given temperature, gives an idea of the average magnitude of static displacements and/or of the amount of particles that took part in the motions once transient displacements (caused by the inherent instability of our system) have settled down. It can, therefore, be used to evaluate the amount of tweed deformations that are taking place in the system at a given temperature. Note that the averaged MSD cannot be meaningful if the diffusion rate in the system is large, since the magnitude of the displacements keeps increasing with time. Fortunately, this was the case only when the vacancy loop was present in the system, and then only at temperatures larger than 4000 K.

We characterized the tweed behavior through the use of calculated diffraction patterns and of plots of the averaged MSD of the particles as a function of temperature. The diffraction patterns were calculated from the instantaneous coordinates of the particles after allowing long enough simulation times to reach equilibrium. We found that the behavior of the system was very much influenced by the temperature at which the simulation was run. This is well illustrated from the diffraction patterns taken in various temperature ranges: At high temperatures ($T \geq 1000$ K), the system shears randomly at all available amplitudes of the shear parameter, and the diffraction pattern appears indistinguishable from that of a perfectly harmonic fcc lattice under these simulation conditions, i.e., peaks at the Bragg positions or slightly away from

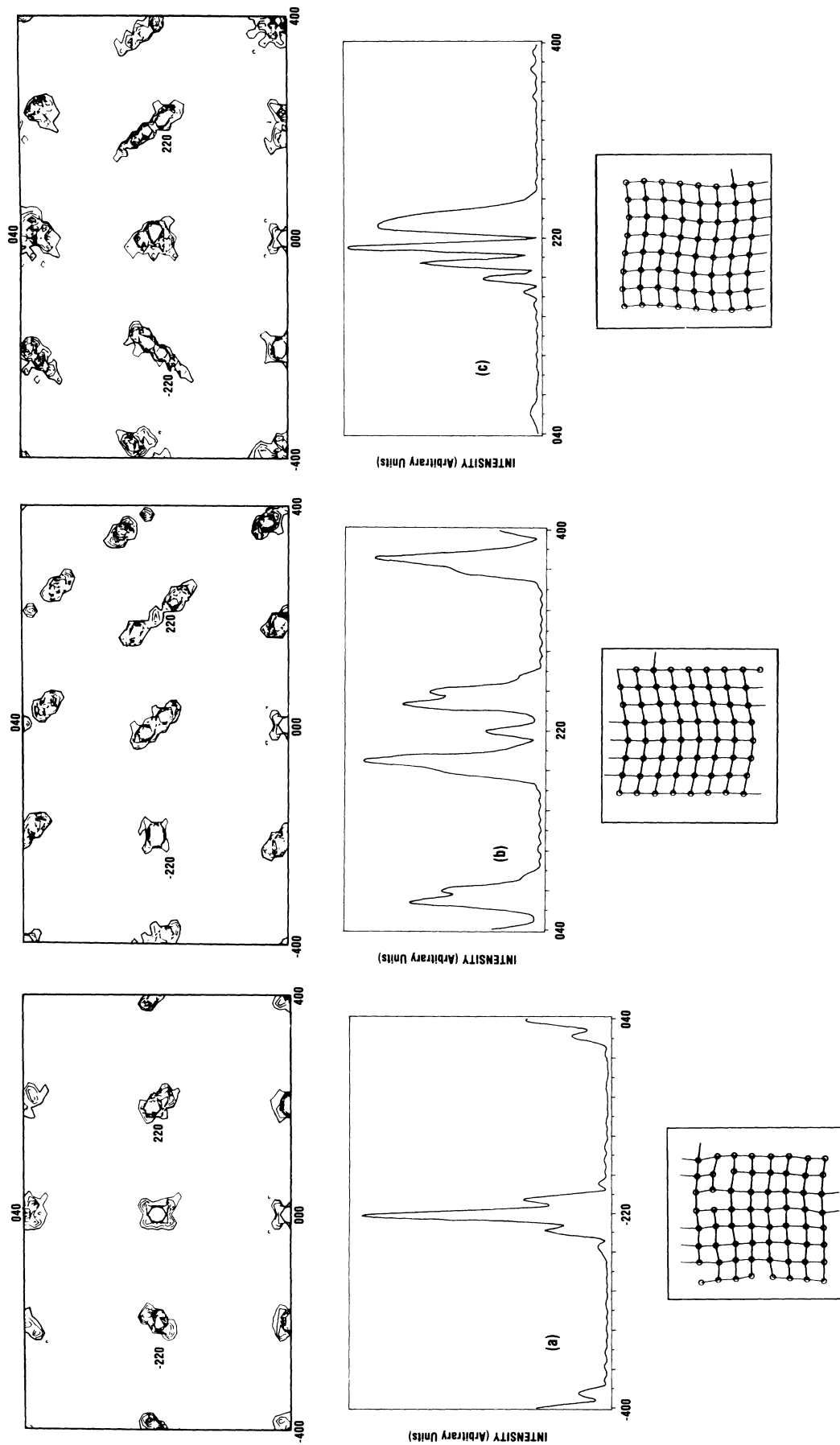


FIG. 4. On top are the calculated diffraction patterns, and on the bottom is represented the corresponding intensity distribution along the (a) $\bar{4}00$ - 040 reciprocal line or (b) and (c) 040 - 400 reciprocal line. (a) Appearance of the tweed at high temperatures. The Bragg peak is only very slightly shifted away from its original position, and the peaks due to the simulation box are hardly visible. (b) Appearance of the tweed at intermediate temperatures. There are two shear peaks located symmetrically around the Bragg position, that are superimposed on the periodic pattern of the simulation box. (c) Appearance of the tweed at very low temperatures. The shear peak appears only on one side of the Bragg position (which is at the position 0.5), whereas the peaks due to the simulation box are symmetrical around that position.

those positions [Fig. 4(a)]. If $30 \leq T < 1000$ K, a scan through one of the (220) peaks of the diffraction pattern reveals that both the positive and negative values of the shear parameter are being activated, which shows as two peaks symmetrical around the original Bragg position [Fig. 4(b)]. In the very low-temperature region ($T < 30$ K), the system is shearing through the use of only one of the two possible values of the shear parameter in that direction, since the Bragg peak is displaced only on one side of the original Bragg position [Fig. 4(c)]. It should be noted that due to the orientation of the simulation box ($Z_{\text{box}} \parallel [001]$), only two out of six distortion modes are allowed in the system: shears along the [110] and the $[1\bar{1}0]$ directions. In the range of temperatures $T < 1000$ K, streaks equivalent to the $\langle 110 \rangle$ streaks that have been reported in the literature started to form in the $\langle 110 \rangle$ directions of the diffraction pattern. Their intensity and length increases upon lowering of the temperature.

In our system, the shear is produced by a periodic shear wave (which is, as a result of the periodic boundary conditions, commensurate with the dimensions of the simulation box) propagating through the box parallel to the edges. In all three cases above, we could identify the periodicity of the subpeaks that appear in the $\langle 110 \rangle$ streaks as artifacts of the periodicity of the simulation box.¹³ A study of the nature of that wave has been conducted and will be discussed later on.

The temperature behavior of the MSD is closely related to the calculated diffraction patterns, as can be seen on a plot of the MSD calculated with reference to step 0 versus temperature (Fig. 5). From 1000 K and up, the

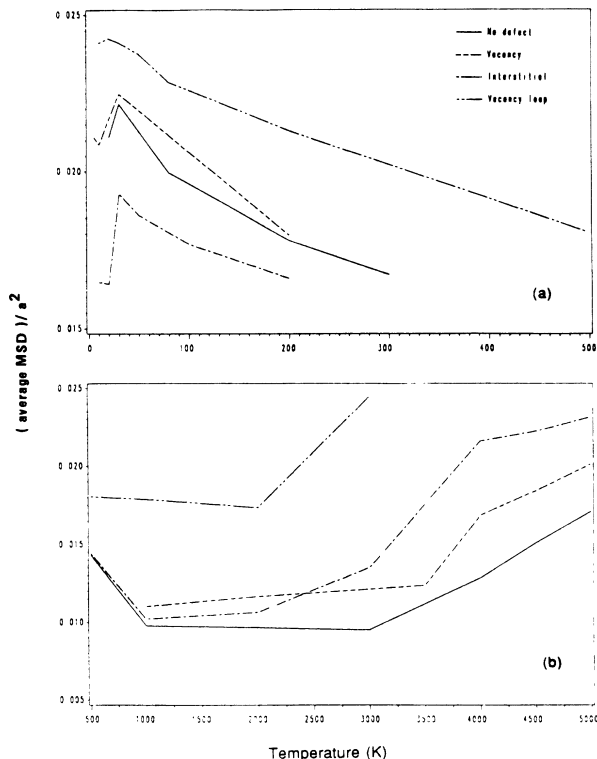


FIG. 5. Mean-square displacement as a function of temperature.

lattice seems to behave as a perfect fcc lattice, where the mean-square displacement increases regularly with temperature. However, below 1000 K, the MSD starts to abnormally increase again, peaks at about 30 K, and decreases slightly for even lower temperatures. This phenomenon occurs with various intensities for all the defects tested.

Our interpretation of the variation of the averaged MSD and the diffraction patterns with temperature is as follows: At high temperatures ($T \geq 1000$ K), thermal energy is sufficient to surmount easily the energy barrier ϵ (Fig. 1), and the system behaves as if it were perfectly harmonic. When the temperature decreases, however, small atomic regions get trapped for longer and longer times in the energy wells that correspond to large values of the strain parameter, hence increasing more and more the time-averaged mean-square displacements of the particles and displacing the Bragg peaks away from the perfect fcc configuration. However, when the temperature becomes less than about 30 K, the thermal energy is so weak that only part of the particles succeed in having displacements large enough to reach one of the energy wells, the other ones remaining more or less around their equilibrium positions. Since the MSD calculation takes all the particles into account, it makes sense that even though some of the particles achieved large displacements, the fact that most remained at their initial positions will decrease the total MSD value.

2. Role of the defects on tweed

It had been proposed^{1,9} that static tetragonal strain fields around defects or precipitates would produce the appearance of tweed. In order to test that suggestion, we introduced various defects into the simulated array, which produce different strain fields. The strain field generated by a vacancy has an essentially cubic symmetry, as does the one produced by the interstitial. The only difference between those two defects is that the vacancy creates a contracting strain field whereas the interstitial creates a dilating strain field. On the other hand, the vacancy loop, which is oriented on a $(1\bar{1}0)$ plane, produces a much more complex strain field which is rather difficult to interpret. However, if we consider the displacements of the atoms that surround the vacancy loop (Fig. 6), either in the layer that contains the loop, or in the layer just above or below it, it seems that the distortions they undergo could be regarded as approximately tetragonal. As shown in Fig. 5, the potency of those defects to produce tweed is variable. A vacancy or an interstitial alone does not seem to produce significantly more tweed (characterized in terms of the averaged mean-square displacement) than what occurs in the perfect-lattice case. It even seems that an interstitial reduces slightly the occurrence of tweed. A vacancy loop, on the other hand, seems to be very effective in producing tweed. The fact that the vacancy loop does indeed produce tetragonal displacements of the atoms substantially larger than those produced by the other defects, as does also the interstitial in the bcc lattice,¹⁴ seems to confirm Tanner's theory that static tetragonal strain fields will bring out the tweed in-

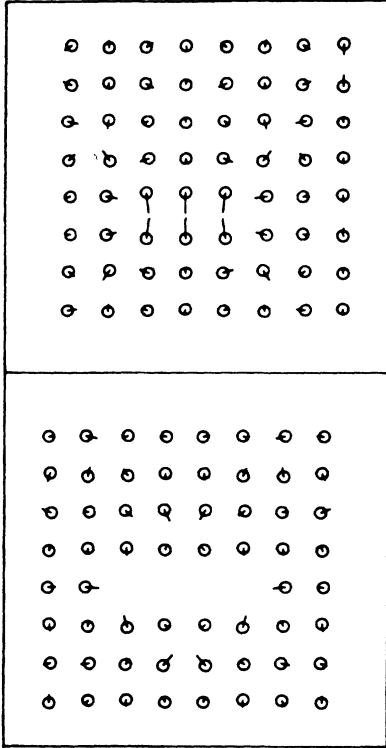


FIG. 6. Perturbations induced during the static relaxation of the lattice containing a vacancy loop. The absolute magnitude of the displacements that occurred during the relaxation process have been increased by a factor 5 to emphasize the pattern of the strain field. The simulation box has been sliced into layers half an fcc unit cell thick in the Z direction, and layers 5 and 6 are represented here.

stability. On the other hand, displacements associated with tweed also appeared in the case of the perfect fcc lattice, or when the lattice contained a vacancy or an interstitial. This thus shows that tweed can form homogeneously as well.

3. Tweed as a premartensitic phenomenon

Even though our system did show tweed at low temperatures, we did not succeed in observing a martensitic transformation in the span of time of the CMD simulations we performed (which was in average about 5000 time steps, 200 average atomic vibration periods, or 1.176×10^{-11} sec), in spite of the expected instability of the fcc phase with respect to the bcc phase as shown by the relative magnitude of their respective lattice potential energies at 0 K (Fig. 2). Even the sheared fcc lattice that produces a static lattice energy of -452.75 K/atom is not as stable as the bcc phase, with an energy of -1938.70 K/atom. (We use the convention of expressing energy in terms of temperature where Boltzmann's constant is an understood multiplicative factor.) This may mean that for kinetic reasons, no martensitic transformation will occur at finite temperature in that system, since it would have to happen at such a low temperature that thermal motions will be much too small to offer any finite probability of surmounting the energy barrier to the

transformation, or that a transformation might still have occurred at the temperatures tested, but was taking longer than the simulation length to nucleate. Yet another explanation may lie in the CMD simulation itself, where the transformation will be aborted if the energy required to create the grain boundary necessary to render the bcc phase commensurate with the simulation box¹⁸ is larger than the driving force for the transformation.

In any case, since all of the interatomic potentials that we calculated to be unstable with respect to (110) shears and that were mechanically stable with respect to both the fcc and the bcc phases also showed the bcc phase to be more stable than the fcc phase at absolute zero. It seems that a tweed instability cannot exist without having a martensitic transformation potentially present in the system.

This result, if true, would not be surprising since bcc may be produced from fcc via the Zener transformation¹⁹ which consists of (1) a $\langle \bar{1}10 \rangle (110)$ shear plus (2) a compression normal to the shear plane, i.e., $\langle 110 \rangle$, and (3) a compression in the $\langle 001 \rangle$ direction, eliminating any remaining tetragonality. The (110) plane of the bcc crystal becomes the (111) plane of the fcc crystal without rotation. Of the three steps of the Zener transformation, the shear usually involves the largest increase in strain energy, so it would seem if this shear mode is already completely soft for small shear amplitudes, the system will be predisposed to a martensitic transformation at some point.

C. Nature of the lowest-energy shear wave

Because of the strong anharmonicity of our potential, we found it of interest to determine the nature of the periodic shear wave traveling through the simulation box. Would it be a classical phonon wave, or would it rather be a nonlinear soliton wave as might be expected from the calculation of Krumhansl and Schrieffer?¹⁵ We decided to calculate dispersion curves for both of those cases and determine their relative energy for the wave vectors corresponding to the dimensions of the simulation box.

As a consequence of the periodic boundary conditions, we had to consider soliton waves made up as the sum of two symmetrical solitons, so that periodicity could be conserved. The waves we investigated are plotted as a function of distance in Fig. 7 and are given below in terms of both their strain and displacement fields:

$$\eta = \mathbf{A}q \cos(\mathbf{q} \cdot \mathbf{r}), \quad \mathbf{u} = \mathbf{A} \sin(\mathbf{q} \cdot \mathbf{r}) \quad (12a)$$

for a phonon, and for the three types of solitons:

$$\eta = \mathbf{A} \quad \text{and} \quad \mathbf{u} = \mathbf{A}r \quad \text{if} \quad r \leq \frac{L_{\text{box}}}{2}, \quad (12b)$$

$$\eta = -\mathbf{A} \quad \text{and} \quad \mathbf{u} = -\mathbf{A} \left[r - \frac{L_{\text{box}}}{2} \right] \quad \text{if} \quad r \geq \frac{L_{\text{box}}}{2}$$

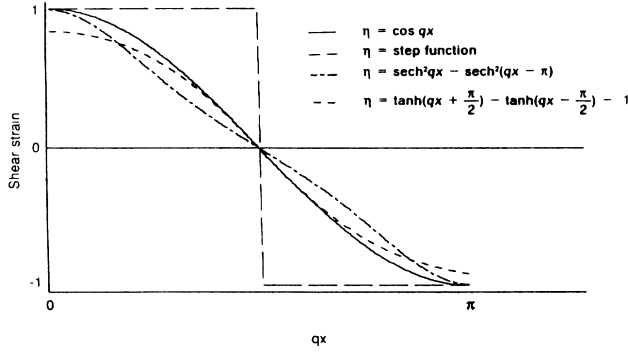


FIG. 7. Strain fields investigated during the study of the shear wave.

for soliton I;

$$\eta = \mathbf{A}q[\tanh(\mathbf{q}\cdot\mathbf{r} - L_{\text{box}}/2) - \tanh(\mathbf{q}\cdot\mathbf{r})], \quad (12c)$$

$$\mathbf{u} = \mathbf{A}[\ln \cosh(\mathbf{q}\cdot\mathbf{r} - L_{\text{box}}/2) - \ln \cosh(\mathbf{q}\cdot\mathbf{r})]$$

for soliton II; and

$$\eta = \mathbf{A}q[\text{sech}^2(\mathbf{q}\cdot\mathbf{r} - L_{\text{box}}/2) - \text{sech}^2(\mathbf{q}\cdot\mathbf{r})], \quad (12d)$$

$$\mathbf{u} = \mathbf{A}[\tanh(\mathbf{q}\cdot\mathbf{r} - L_{\text{box}}/2) - \tanh(\mathbf{q}\cdot\mathbf{r})]$$

for soliton III. The wave vector \mathbf{q} was chosen parallel to the $[1\bar{1}0]$ direction, and the amplitude vector \mathbf{A} parallel to the $[110]$ direction. L_{box} is the length of the CMD simulation box in the direction of propagation of the wave. For the solitons a different simulation box has been used, on which no periodic boundary conditions were imposed, that consisted of one unit cell in the $[110]$ and 10 unit cells in the $[1\bar{1}0]$ direction, the direction of propagation of the soliton [Fig. 8(a)].

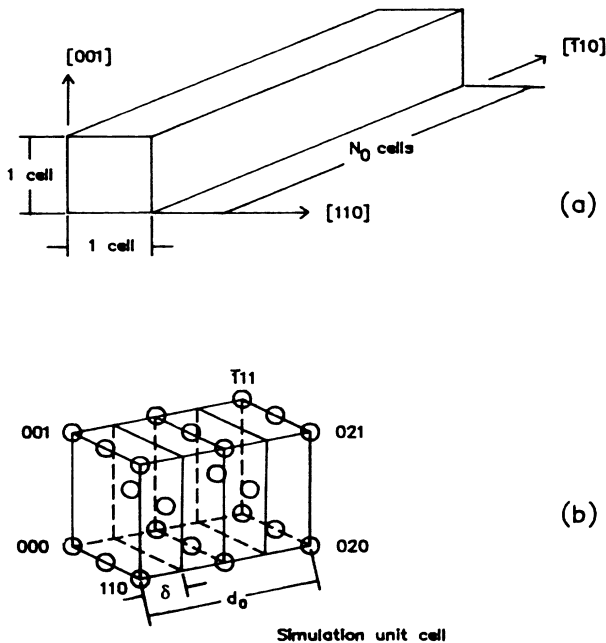


FIG. 8. Simulation cell used for the dispersion calculations. (a) Orientation of the simulation cell; (b) details of one fcc unit cell.

For phonon calculations the length of the simulation box in the direction of propagation of the wave is directly related to the precision desired on the dispersion curve, since the only allowed wave vectors are such that

$$q = \frac{2\pi n}{N_0 d_0} = \frac{2\pi n}{N_0 m \delta}, \quad n=0,1,2,\dots,\frac{mN_0}{2}, \quad (13)$$

where q is the wave vector, N_0 is the number of unit cells in the direction of propagation of the wave, d_0 is the length of the unit cell in the direction of propagation of the wave, δ is the spacing between planes perpendicular to the direction of the wave, and m is the number of those planes within one unit cell [see Fig. 8(b)]. Higher values of n would lead to values of q greater than the limit of the first Brillouin zone $q_{\text{max}} = \pi/\delta$. In the case of an fcc unit cell of lattice parameter a_0 , $d_0 = 4\delta = a_0\sqrt{2}$, and for phonons $N_0 = 4$ was found to give sufficient accuracy for our purposes.

We calculated the dispersion curves for amplitudes between 5% and 30% of the fcc lattice parameter a_0 . The potential energy corresponding to each wave vector is calculated as follows.

(1) The displacements of the particles under the influence of the wave are calculated, and the new positions stored in the array.

(2) The interaction energy of each particle with all of its neighbors is computed using the interatomic potential

$$E_i = \frac{1}{2} \sum_{j (\neq i)} V(r_{ij}). \quad (14)$$

(3) The total energy per atom is finally calculated

$$E = \frac{1}{N} \sum_{i=1}^N E_i, \quad (15)$$

where N is the total number of particles in the simulation box.

In the case of the phonon wave, we found necessary, especially at high- q values, to additionally phase average the energy of the wave to ensure the reproduction of the effect of a wave traveling through the crystal. Phase averaging was performed by averaging, for a given value of the amplitude and wave vector, the energies calculated for a wave whose phase angle at the origin varies between 0 and 2π by increments of $1/16\pi$.

The results are shown in Figs. 9(a)–9(c). The results obtained in the case of the soliton wave I, which only depends on an amplitude term and is independent of any wave-front factor, are listed in Table II. The energy maximum that occurs for the larger amplitudes at $q/q_{\text{max}} = 0.5$ can be rationalized if one considers the particle displacements produced by such a wave. Indeed, every other plane of atoms will have a maximum displacement, while the remaining planes will not be displaced at all. For large amplitudes (greater than about 20% of the lattice spacing), both situations correspond to a maximum in energy, while at smaller amplitudes, the magnitude of the displacements (when they occur) pro-

duces a decrease in the corresponding lattice energy.

In the case of phonons, the only allowed q values are those that are commensurate with the CMD simulation box size L_{box} . Since $L_{\text{box}} = 4d_0 = 16\delta$, we must, therefore, have values of the wavelength $\lambda = 16\delta, 8\delta, 4\delta,$ and 2δ , i.e., $q/q_{\text{max}} = 0.125, 0.25, 0.5,$ and 1 . The lowest-energy phonon in our array would have, out of those four al-

lowed values, the combination of wave vector and amplitude that generates the lowest lattice energy. Observation of Fig. 9(a) shows that the most stable phonon in our system would have a wavelength equal to the length of the box L_{box} and an amplitude of about 20% of the lattice spacing, with an energy of about -120 K/atom. Note that this amplitude corresponds exactly to the value

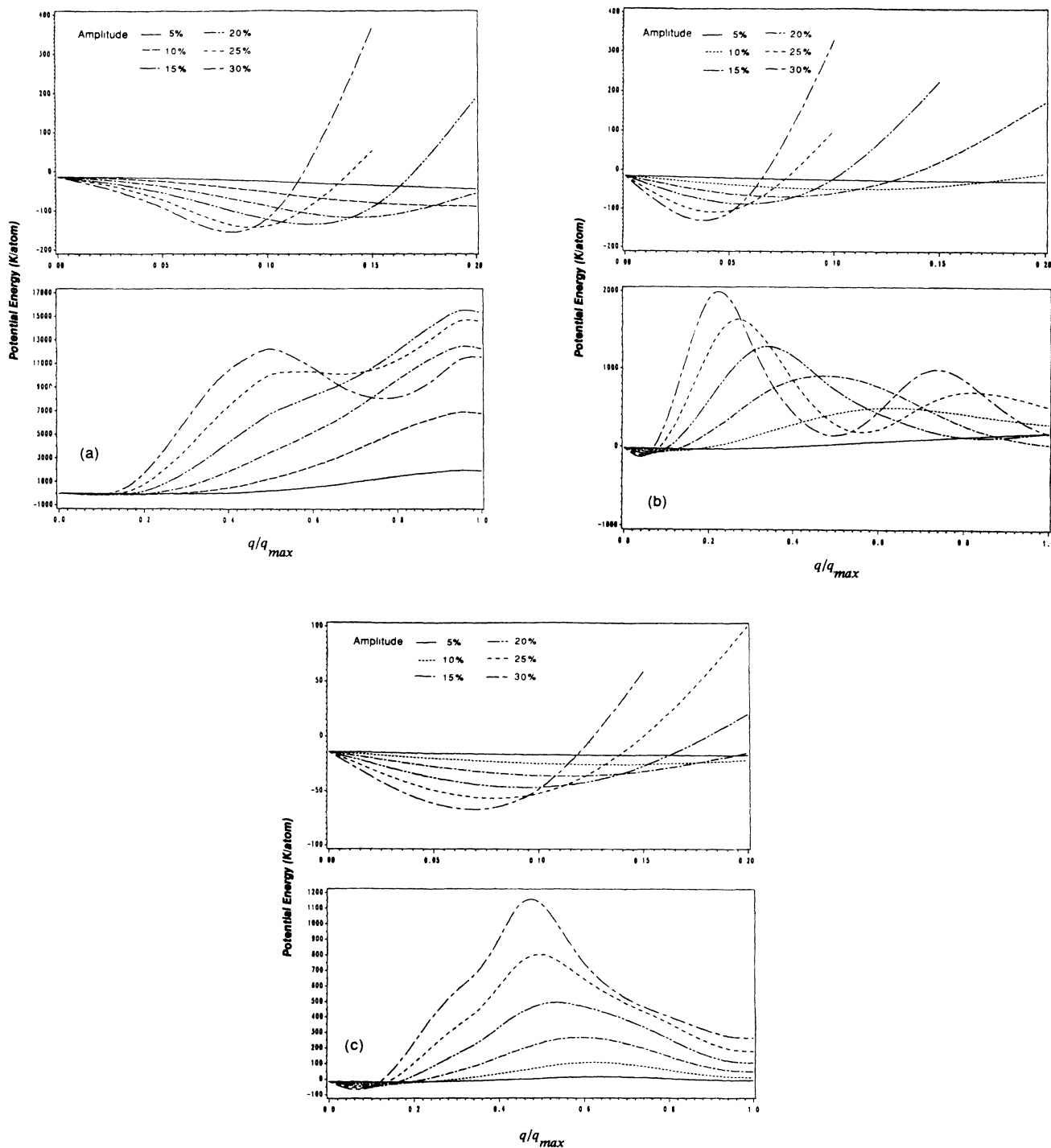


FIG. 9. Results of the dispersion calculations. (a) Phonon wave. (b) Soliton II. (c) Soliton III. Top figures represent a blowup of the energy behavior at small wave vectors. The energy is in units of kelvin, and the amplitude is in percentage of the fcc lattice parameter.

TABLE II. Results obtained in the case of the propagation of a step-function wave.

Amplitude (in % of the lattice parameters, a_0)	Lattice energy (K/atom)
5	-30.325
10	-67.732
15	-95.847
20	-67.465
25	77.697
30	390.751

of the shear-strain parameter at the minima of the potential energy curve.

On the other hand, all the soliton waves tested were already commensurate with the simulation box, and the parameter q is now only an indication of the steepness of the change in the strain field as a function of distance. The lattice energy produced by the step-function strain-field wave (soliton I) is always larger than the lowest-energy phonon described above, so that it is not very probable that such a wave would propagate in our system. Figure 9(b) and 9(c) indicate that a steep change in the strain field (high q) is a very unfavorable configuration since all these waves would yield an increase in the energy of the system. However, the more gradual changes of the strain fields achieved with values of q below about 0.2 for solitons II and III produce a lowering of lattice energy with the minima occurring at $q \cong 0.04$ and 0.07 for II and III, respectively, and an amplitude of about 30% in each case. For increases in the amplitude above 30% (not shown) the lattice energy begins to increase again, so that 30% is about optimum. In comparing the minimum energies reached by each type of soliton, one finds -95, -130, and -65 K/atom for solitons I, II, and III, respectively. A rough estimate may be made of the soliton interfacial energies by regarding the difference between the above numbers and the ground-state energy of -453.90 K/atom as a measure of the excess energy of the two soliton wave fronts per simulation box. Given that the simulation box contained 80 atoms and had a cross sectional area of $\sqrt{2}a_0^2$, these estimates are 10 150, 9165, and 11 000 K/ a_0^2 per wave front in the same order.

Consequently, we have good reasons to believe that the wave that dominates the displacive motion in our solid at low temperatures is indeed a soliton wave of type II described in Eq. (12c). This result is particularly interesting for two reasons. First, it confirms the results obtained by Krumhansl¹⁵ that soliton waves will provide important components of the motion in highly anharmonic solids, and second, we found a stable form of soliton wave that to our knowledge has not been considered before (type II). If we were to increase the size of the simulation box, the energy/atom of the phonon wave will decrease slightly, but that of the solitons will decrease even more. In the limit of an infinite box size, the energy of soliton II would reach the value of -453.90 K/atom.

IV. CONCLUSION

In view of the two parallel main theories of tweed, it appears to us that tweed can indeed be divided into two

categories: a *static tweed*, which occurs in the vicinity of microstructural features in the crystal, and which seems to originate principally from the elastic properties of the material, and in particular its anisotropy, and a *dynamic tweed*, which has for cause a strong lattice anharmonicity in a certain temperature range. Our approach to the treatment of tweed instabilities restricts the extent of our interpretation of the tweed phenomenon to the second category. In that context, we found the following conclusions.

(1) As opposed to bcc crystals, there are no easily recognizable features of the geometrical shape of the interatomic potentials of fcc crystals that show a tweed instability that could help distinguish them from normal materials.

(2) There is some evidence that the presence of a tweed instability in the system implies the potential of a martensitic transformation, whether or not that transformation is kinetically possible. In other words, it seems that tweed is indeed a premartensitic phenomenon.

(3) Tweed can nucleate homogeneously, but the presence of tetragonal strain fields in the lattice will enhance its formation.

In addition, we identified the elastic shear wave that propagates in such an anharmonic solid as being a soliton, whose displacement field has the form

$$\mathbf{u} = \frac{\mathbf{A}}{q} \ln \cos(\mathbf{q} \cdot \mathbf{r}) .$$

ACKNOWLEDGMENTS

We would like to thank Jon Rifkin for his very kind help with the computer graphics. The support of a U. S. Department of Energy (DOE) contract through Lawrence Livermore National Laboratory monitored by Dr. L. E. Tanner, and also some support of the National Science Foundation (NSF), through its Division of Materials Research, is gratefully acknowledged.

APPENDIX: FOURIER EXPANSION OF A CURVE WITH A DOUBLE MINIMUM

In this section, we derive the minimal number of parameters of a Fourier expansion required to produce a curve $E(\eta)$ with a double minimum around $\eta=0$ that is periodic of period η_0 . Let us assume that the minima are located at $\eta = \pm \epsilon$ ($\epsilon \geq 0$). Then, the condition of a double minimum requires that

$$\left. \frac{dE}{d\eta} \right|_{\eta = \pm \epsilon} = 0 \quad (\text{A1})$$

and

$$\left. \frac{d^2E}{d\eta^2} \right|_{\eta = \pm \epsilon} > 0 . \quad (\text{A2})$$

The function $E(\eta)$ is even, therefore the Fourier expansion is limited to the cosine series:

$$E(\eta) = \sum_n A_n \cos \left[\frac{2\pi n \eta}{\eta_0} \right] . \quad (\text{A3})$$

Thus the first derivative with respect to η is

$$\frac{dE}{d\eta} = -\frac{2\pi}{\eta_0} \sum_n n A_n \sin \left[\frac{2\pi n \eta}{\eta_0} \right], \quad (\text{A4})$$

and the second derivative is

$$\frac{d^2E}{d\eta^2} = -\left[\frac{2\pi}{\eta_0} \right]^2 \sum_n n^2 A_n \cos \left[\frac{2\pi n \eta}{\eta_0} \right]. \quad (\text{A5})$$

So, for a double minimum at $\eta = \pm \varepsilon$, we want

$$\sum_n n A_n \sin \left[\frac{2\pi n \varepsilon}{\eta_0} \right] = 0, \quad (\text{A6a})$$

$$\sum_n n^2 A_n \cos \left[\frac{2\pi n \varepsilon}{\eta_0} \right] < 0. \quad (\text{A6b})$$

Case 1, when $n = 0, 1$. Equation (A6a) can be rewritten as

$$A_1 \sin \left[\frac{2\pi \varepsilon}{\eta_0} \right] = 0 \quad (\text{A7})$$

which holds if

$$A_1 = 0 \text{ or } \varepsilon = k \frac{\eta_0}{2}, \quad k \text{ an integer.} \quad (\text{A8})$$

The case $A_1 = 0$ is trivial and is of no interest for the problem. The other solution tells us that it is possible to describe a curve with a double minimum with only two elements in the Fourier series A_0 and A_1 under the condition that $\varepsilon \geq \eta_0/2$. However, this case is not of practical interest for us, since in our particular application, we would rather have the minimum located close to the origin.

Case 2, when $n = 0, 1, 2$. Equation (A6a) can be rewritten as

$$A_1 \sin \left[\frac{2\pi \varepsilon}{\eta_0} \right] + 2A_2 \sin \left[\frac{4\pi \varepsilon}{\eta_0} \right] = 0 \quad (\text{A9})$$

which can be solved if

$$\frac{A_1}{4A_2} = -\cos \left[\frac{2\pi \varepsilon}{\eta_0} \right]. \quad (\text{A10})$$

If $0 \leq \varepsilon \leq \eta_0/4$, then $\cos(2\pi\varepsilon/\eta_0) \geq 0$, and A_1 and A_2 must be of opposite signs. If $\eta_0/4 \leq \varepsilon \leq \eta_0/2$, then A_1 and A_2 must be of the same sign.

Inserting Eq. (A10) into Eq. (A6b) gives

$$4A_2 \left[\frac{A_1^2}{(4A_2)^2} - 1 \right] < 0 \quad (\text{A11})$$

which can also be written as

$$-4A_2 \sin^2 \left[\frac{2\pi \varepsilon}{\eta_0} \right] < 0 \quad (\text{A12})$$

which is possible only if $A_2 > 0$. Since we require that the minima be close to the origin, we must have $A_1 \leq 0$. If we further add the condition that $E(0) = 0$, then we must have

$$\sum_n A_n = 0 \quad (\text{A13})$$

or, in this case,

$$A_0 + A_1 + A_2 = 0. \quad (\text{A14})$$

In conclusion, a periodic curve with a double minimum located close to the origin can be described by a Fourier expansion limited to three terms. The knowledge of one of the expansion coefficients allows the determination of the two remaining ones, through the relations (A10) and (A14).

¹L. E. Tanner, *Philos. Mag.* **14**, 111 (1966).

²Xie Sishen *et al.*, *J. Phys. D* **20**, 807 (1987).

³J. Yu, A. J. Freeman, and J. H. Xu, *Phys. Rev. Lett.* **58**, 1035 (1987).

⁴I. M. Robertson and C. M. Wayman, *Philos. Mag. A* **48**, 421 (1983).

⁵K. Otsuka, C. M. Wayman, and H. Kubo, *Metall. Trans. A* **9**, 1075 (1978).

⁶Yu. D. Tyapkin *et al.*, *Phys. Met. Metallogr. (USSR)* **41**, 123 (1976).

⁷S. F. Dubinin *et al.*, *Phys. Status Solidi A* **67**, 75 (1981).

⁸I. M. Robertson and C. M. Wayman, *Philos. Mag. A* **48**, 443 (1983).

⁹S. H. Wen, A. G. Khatchaturyan, and J. W. Morris, Jr., *Metall. Trans. A* **12**, 581 (1981).

¹⁰L. Delaey, P. F. Gobin, G. Guénin, and H. Warlimont, in

Proceedings of the International Conference on Martensitic Transformations, ICOMAT-1979, MIT, Cambridge, MA, p. 400.

¹¹G. Guénin and P. F. Gobin, in Ref. 10, p. 532.

¹²G. Haush and R. Warlimont, *Acta Metall.* **21**, 401 (1973).

¹³M. Foos, C. Frantz, M. Gantois, in Ref. 10, p. 485.

¹⁴P. C. Clapp, J. Rifkin, J. Kenyon, and L. E. Tanner, *Metall. Trans. A* **19**, 783 (1988).

¹⁵J. A. Krumhansl and J. R. Schrieffer, *Phys. Rev. B* **11**, 3535 (1975).

¹⁶P. Deymier and G. Kalonji, *J. Chem. Phys.* **85**, 2937 (1986).

¹⁷K. Maeda, V. Vitek, and A. P. Sutton, *Acta Metall.* **30**, 2001 (1982).

¹⁸A. Silberstein, Ph.D. thesis, University of Connecticut, 1987.

¹⁹J. Rifkin, *Philos. Mag. A* **49**, L31 (1984).